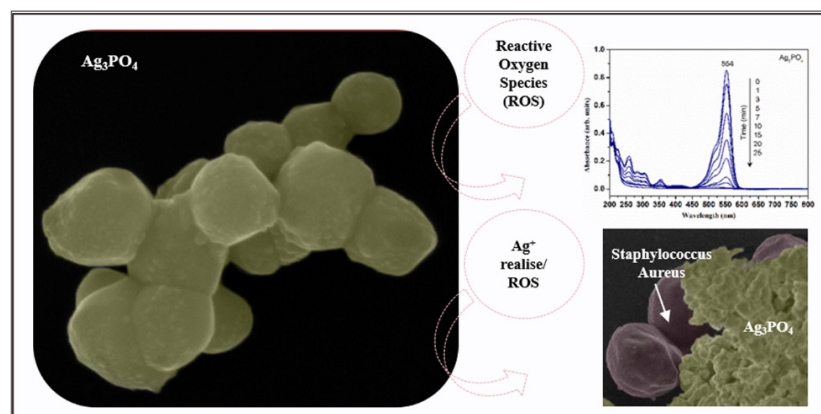# Photocatalytic Activity and Antibacterial Effect of Ag₃PO₄ Powders Against Methicillin-resistant *Staphylococcus aureus*

Gleice Botelho* [a], Camila Cristina de Foggi [b], Carlos Eduardo Vergani [b], Wyllamanney Silva Pereira [c], Ricardo Kaminishi dos Santos Júnior [a], and Elson Longo [c]

In this study, silver phosphate (Ag₃PO₄) was successfully prepared through a simple precipitation method, and its structural, optical, and morphological properties were characterized by X-ray diffraction, Rietveld refinement, Fourier transform infrared spectroscopy, UV−vis diffuse reflectance spectroscopy, photoluminescence measurements, and field emission scanning electron microscopy (FE-SEM). Thereafter, the photocatalytic activity for the degradation of rhodamine B (RhB) dye and the antibacterial effect against methicillin-resistant Staphylococcus aureus (MRSA) were analyzed. Ag₃PO₄ was highly photocatalytic, degrading approximately 100% of the RhB after 25 min of visible light exposure. The photocatalytic mechanism was evaluated by trapping experiments indicating that photogenerated holes and superoxide radicals were the principal species present in the photocatalytic system. In addition, Ag₃PO₄ is a potential bacterial agent as it reduced the MRSA population even at sub-inhibitory concentrations. Morphological changes of the MRSA cells exposed to Ag₃PO₄ powder were investigated by the FE-SEM analysis, and a possible mechanism involving the release of dissolved Ag⁺, together with the production of reactive photocatalytic oxygen species is proposed based on the experimental results.

Graphical abstract

1. Introduction

Silver orthophosphate (Ag₃PO₄) is a well-known, visible-light-driven photocatalyst and a p-type semiconductor with an indirect band gap of 2.36 eV [1]. It has attracted widespread attention for harvesting solar energy for environmental remediation and energy conversion due to its relatively narrow band gap, strong optical absorption, low toxicity, excellent

[a] Department of Environmental Chemistry, Federal University of Tocantins, P.O. Box 66, 77402-970, Gurupi, TO, Brazil. [b] Department of Dental Materials and Prosthodontics, São Paulo State University, P.O. Box 355, 14801-903, Araraquara, SP, Brazil. [c] INCTMN-UFSCar, Federal University of São Carlos, P.O. Box 676, 13565-905, São Carlos, SP, Brazil. *Corresponding author. E-mail: **gleice.lorena@mail.uft.edu.br**

quantum efficiency, and high photoactivity [1-4]. The first publication on the environmental remediation ability of Ag$_3$PO$_4$ was performed by Yi et al. [3] in 2010. They analyzed the decomposition of methylene blue dye in aqueous solution under visible-light irradiation. Subsequently, this semiconductor was widely studied for degrading a wide variety of organic contaminants from different sources including agrochemical, agricultural, and pharmaceutical effluents [5-9].

Antimicrobial activity is another important property of Ag$_3$PO$_4$ [10-16]. The study and development of antimicrobial agents is necessary because of the resistance of certain microorganisms to commonly used antimicrobials such as levofloxacin, penicillin, aminoglycosides, macrolides, cephalosporin (first, second, and third generation), vancomycin, metronidazole, trimethoprim/sulfamethoxazole, and beta-lactam antibiotics. For example, the emergence of the bacterial strain of S. aureus—resistant to the effect of antibiotics—during infection outbreaks among hospitalized patients is a serious problem worldwide. Several of the risk factors for the development of methicillin-resistant Staphylococcus aureus (MRSA) infections in humans include previous surgery, immunosuppression, and the indiscriminate use of antimicrobials [17]. Ag-containing materials have several active antimicrobial mechanisms and represent excellent alternatives to existing antimicrobials [18-22] as it is unlikely that microorganisms will develop resistance to them [23, 24].

Our team has recently dedicated significant resources to the study of the structural, morphological, optical, and photocatalytic (PC) properties of Ag$_3$PO$_4$ microcrystals using a combination of theoretical calculations and experimental techniques [25,26]. In this work, we furthered those studies and synthesized an Ag$_3$PO$_4$ sample by a simple precipitation method. The structures and morphologies were characterized using experimental techniques such as X-ray diffraction (XRD) with Rietveld analysis, Fourier-transform infrared (FTIR) spectroscopy, field-emission scanning electron microscopy (FE-SEM), UV-vis diffuse reflectance spectroscopy (DRS), and photoluminescence (PL) measurements. Subsequently, the PC properties of Ag$_3$PO$_4$ were investigated together with its antibacterial effect against MRSA by proposing possible mechanisms of antibacterial activity and determining minimum inhibitory/bactericidal concentrations (MIC/MBC).

2. Results and Discussion

Characterization

The typical XRD pattern of the Ag$_3$PO$_4$ powder in Figure 1 shows sharp and well-defined peaks. These diffraction peaks can be indexed as body-centered cubic structures with $P4\bar{3}n$ and space-group symmetry in agreement with the Inorganic Crystal Structure Database (ICSD) No. 14000 [28]. No deleterious phase peaks were found in the sample. It is difficult to draw conclusions on the presence of Ag nanoparticles on the surface of this material from XRD measurements because of the low detection limit of this technique ($\approx$ 3%). The Rietveld analysis confirmed these results **(Supplementary Information Figure S1 and Tables S1–S2)**.

Figure 2 shows the FTIR spectrum in the 400−4000 cm^{-1} range. Analyzing the results renders the presence of eight FTIR active modes, which agrees with the information

reported in prior literature [26, 29-31]. The absorption bands at 3404 and 1664 cm^{-1} — caused by the presence of water molecules adsorbed on the surfaces of the samples — correspond to O−H stretching and H−O−H bending vibrations, respectively. The remaining bands are associated to the PO$_4^{3-}$ groups. Thus, the observed absorption bands are: the asymmetric stretching mode of the PO$_4^{3-}$ group at 1074 cm^{-1} and 1012 cm^{-1}, the symmetric stretching mode of the P-O bonds at 859 cm^{-1}, and the bending mode of the P−O−P bonds at 674 cm^{-1} and 545 cm^{-1} [32-36]. The band at about 1402 cm^{-1} can be associated to the nitrate impurities as AgNO$_3$ precursor used for the synthesis of photocatalyst [31-37].
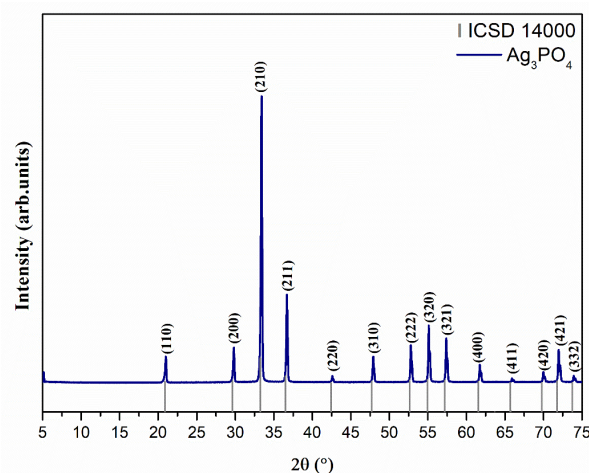

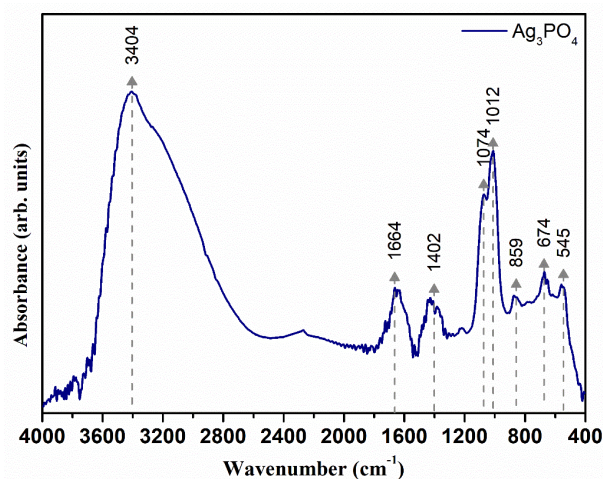**Fig. 1**. XRD pattern of Ag$_3$PO$_4$ powders.

Fig. 2. FTIR spectrum of Ag$_3$PO$_4$ powders.

Figure 3(a) illustrates the FE-SEM images of the Ag$_3$PO$_4$ samples that show several irregular spherical-like agglomerated microparticles. Average particle size was estimated from the FE-SEM micrographs by counting 200 microparticles with good surface contours (**Supplementary Information Figure S2**). The particle sizes were well described by the log normal distribution, presenting an average size of 0.289 ± 0.005 μm. Figure 3(b) illustrates the presence of several irregular nanostructures (dotted white circles) on the surface of the Ag$_3$PO$_4$ microparticles. According to our previous research on Ag$_3$PO$_4$, these nanostructures are composed of Ag nanoparticles and can be active growth nuclei when stimulated by an external source such as the

electron beam of a SEM instrument [25]. This phenomenon was observed for other inorganic Ag-containing materials [38-42]. This information is relevant because several studies show that the optimal amount of Ag nanoparticles can favor, for example, the PC performance of a material because of surface plasmon resonance (SPR) that contributes to the effective charge separation in a semiconductor [31, 43, 44]. In

this context, Yan et al. [31] successfully synthesized Ag_3PO_4 containing Ag nanoparticles and high Ag vacancies. The enhanced photocatalytic activity of this material was associated with the synergistic effect of the Ag vacancies and Ag nanoparticles that contributed to the efficient separation of photogenerated charge carriers.
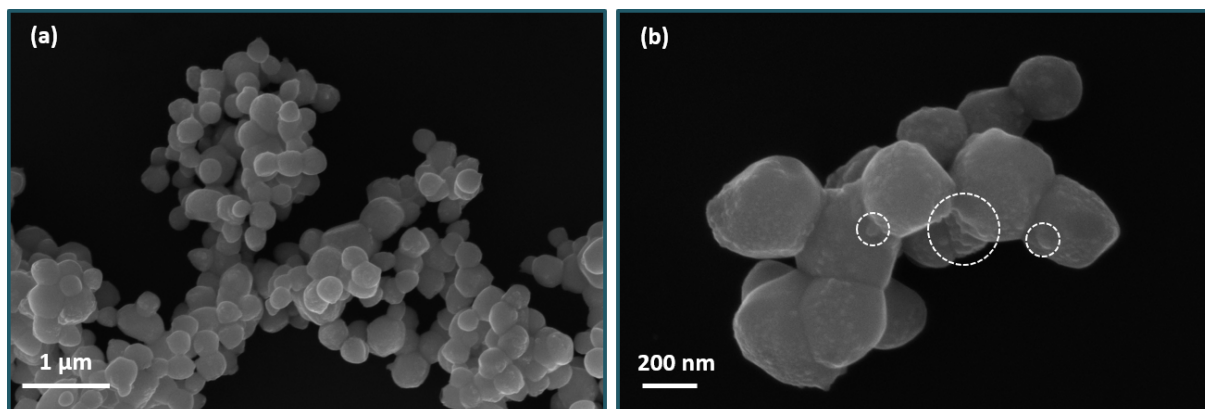

Fig. 3. (a) Low-magnification and (b) high-magnification FE-SEM images of Ag_3PO_4.

The optical properties of a material are important for PC activity. We utilized UV-vis DRS to investigate the optical properties of Ag_3PO_4 and to provide information on the band gap energy (E_{gap}), the formation process of photoinduced electrons (e^-) and holes (h^+) between the valence band (VB) and the conduction band (CB). From the UV-vis spectrum, the E_{gap} of Ag_3PO_4 was determined according to the method proposed by Wood and Tauc [45] using the Kubelka-Munk (K-M) function [46] described in the **Supplementary Information**. The E_{gap} value of 2.29 eV determined from Figure S3 agrees with prior literature [3, 5, 8] and indicates that Ag_3PO_4 has a high PC potential in the visible light region.

Photocatalytic activity measurements

The PC activity of Ag_3PO_4 was evaluated using the degradation of RhB solutions under visible light irradiation. The variations in the maximum absorption band (Figure 4(a)) of the dye solutions was monitored and showed a reduction of approximately 100% in the maximum absorption spectra. Moreover, no new absorption bands were created in the UV-vis spectra in the 200−800 nm range, suggesting that the high percentage of RhB was photodegraded without the simultaneous formation of secondary products. Photolysis of RhB in the absence of Ag_3PO_4 showed a negligible degree of degradation after 25 min of exposure. The insets in Figure 4(a) and 4(b) present the digital images of the RhB solutions after different exposure times to visible light irradiation in the presence and absence of Ag_3PO_4, respectively.

The discoloration curves confirm that the RhB solution was completely degraded after 25 min in the presence of Ag_3PO_4 (Figure 4(c)). The kinetics of the reaction were evaluated to obtain more information on the photodegradation process. Applying a pseudo-first order model, the photocatalytic reaction can be described by:

$$-\ln[C]_t/[C]_0 = kt \qquad (1)$$

where $[RhB]_t$ is the concentration of the dye solution at different times (t), $[RhB]_0$ is the initial concentration of the dye solution, and k is the degradation rate constant. According to equation (1), the first-order rate constant values for the

photodegradation of RhB in the presence and absence of Ag_3PO_4 are 0.2314 and 1.11×10^{-3} min^{-1}, respectively (Figure 4(d)). The correlation coefficient (R^2) and standard deviation (SD) statistically confirm that a pseudo-first order mechanism can describe the photodegradation of RhB.

Recent studies on the Ag_3PO_4 have shown promising results for degradation of organic contaminants under visible light compared with other pure compounds. For example, Qi et al. [47] observed that the photocatalytic process with Ag_3PO_4 was 5.6 times faster than with $BiVO_4$, known as a typical visible light photocatalyst. Similarly, Saud et al. [48] observed that Ag_3PO_4 degraded almost 80% of methylene blue dye within 20 minutes, however the MoS_2 degraded only 34% under the same experimental conditions. The studies on other visible light photocatalyst produced similar results [49-50].

The PC mechanism for the degradation of dye molecules is complex; however, free radicals such as hydroxyl ($OH^•$), superoxide ($O_2^{•-}$), and hydroperoxyl ($HO_2^•$) usually participate in the process [2]. Experiments were conducted to identify the response of primary oxidant species to PC activity and to properly understand the possible degradation mechanism of the RhB solution (Figure 5). ISO and BQ were used as scavengers in these experiments to capture $OH^•$ and $O_2^{•-}$ radicals, respectively. AO was used to capture the photogenerated h^+ [43]. The experimental results illustrate that ISO did not affect the percentage of degraded RhB. Figure 5 shows that BQ and AO reduce degradation to approximately 85 and 36%, respectively. Therefore, $O_2^{•-}$ radicals and holes contribute to photocatalytic performance whereas $OH^•$ radicals do not. The holes in the VB of the Ag_3PO_4 are the main reactive oxidizing species due their highly positive potential and can react directly with RhB [2]. Theoretically, the $O_2^{•-}$ radical could not be generated in this PC process because the reduction potential for the formation this radical is more negative than that of CB in Ag_3PO_4. However, several studies report the participation of $O_2^{•-}$ radicals in the Ag_3PO_4 photocatalytic process [51-55], as demonstrated by Yang et al. [55] and Yang et al. [54] using the electron spin resonance method of radical detection. According to prior literature, the SPR effect and excess-electron-accumulation may result in the production of $O_2^{•-}$ radicals and, therefore, affect
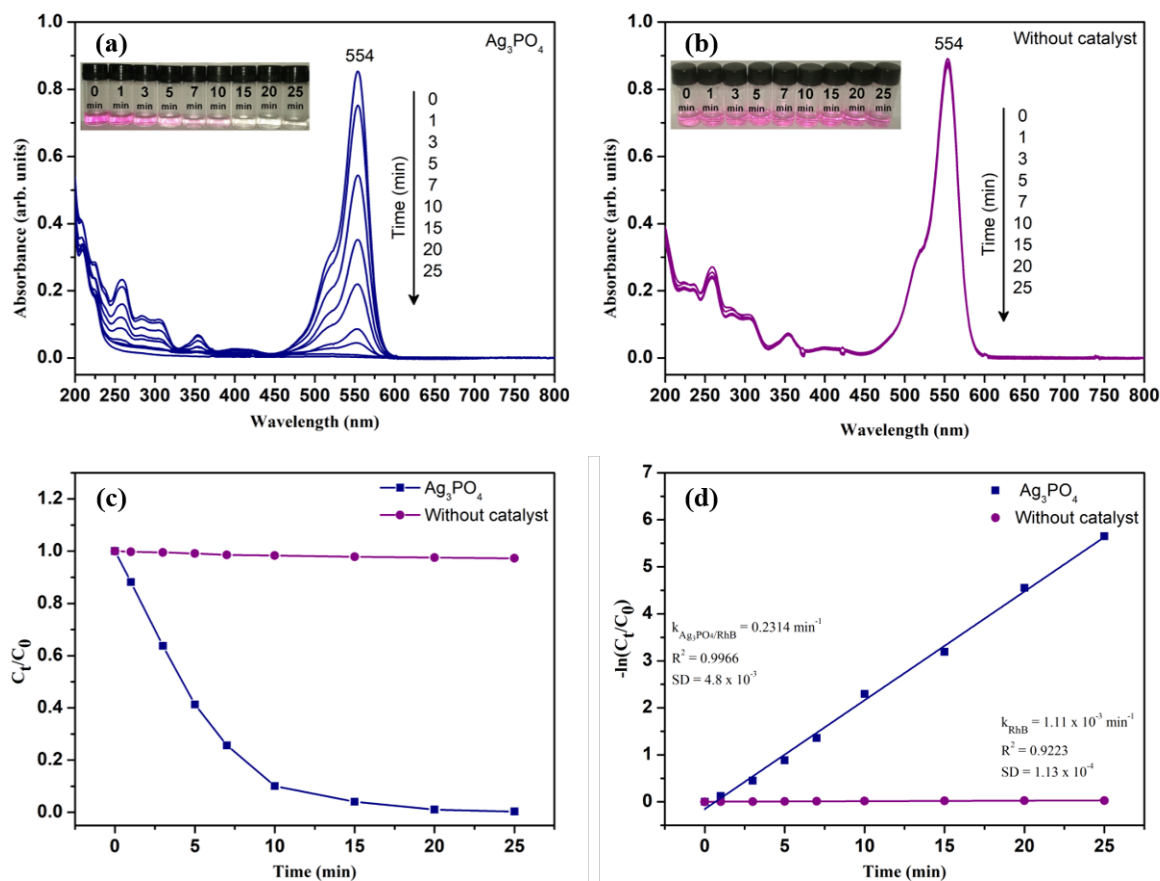
photocatalytic activity [2].

Fig. 4. UV-vis absorption spectra of RhB solutions under visible light irradiation (a) with Ag_3PO_4 and (b) without a catalyst. The insets show digital images of post-irradiated RhB. (c) Discoloration curves and (d) first-order kinetics with and without catalysts.

Recent studies on the Ag_3PO_4 have shown promising results for degradation of organic contaminants under visible light compared with other pure compounds. For example, Qi et al. [47] observed that the photocatalytic process with Ag_3PO_4 was 5.6 times faster than with $BiVO_4$, known as a typical visible light photocatalyst. Similarly, Saud et al. [48] observed that Ag_3PO_4 degraded almost 80% of methylene blue dye within 20 minutes, however the MoS_2 degraded only 34% under the same experimental conditions. The studies on other visible light photocatalyst produced similar results [49-50].

The PC mechanism for the degradation of dye molecules is complex; however, free radicals such as hydroxyl ($OH^•$), superoxide ($O_2^{•-}$), and hydroperoxyl ($HO_2^•$) usually participate in the process [2]. Experiments were conducted to identify the response of primary oxidant species to PC activity and to properly understand the possible degradation mechanism of the RhB solution (Figure 5). ISO and BQ were used as scavengers in these experiments to capture $OH^•$ and $O_2^{•-}$ radicals, respectively. AO was used to capture the photogenerated h^+ [43]. The experimental results illustrate that ISO did not affect the percentage of degraded RhB. Figure 5 shows that BQ and AO reduce degradation to approximately 85 and 36%, respectively. Therefore, $O_2^{•-}$ radicals and holes contribute to photocatalytic performance whereas $OH^•$ radicals do not. The holes in the VB of the Ag_3PO_4 are the main reactive oxidizing species due their highly positive potential and can react directly with RhB [2]. Theoretically, the $O_2^{•-}$ radical could not be generated in this PC process because the reduction potential for the formation this radical is more

negative than that of CB in Ag_3PO_4. However, several studies report the participation of $O_2^{•-}$ radicals in the Ag_3PO_4 photocatalytic process [51-55], as demonstrated by Yang et al. [55] and Yang et al. [54] using the electron spin resonance method of radical detection. According to prior literature, the SPR effect and excess-electron-accumulation may result in the production of $O_2^{•-}$ radicals and, therefore, affect photocatalytic activity [2].

The FE-SEM images (Figure 3(b)) illustrated the presence of a small amount of Ag nanoparticles on the Ag_3PO_4 surface; moreover, Ag nanoparticles can also be formed from the self-photoreduction of Ag_3PO_4 during the photocatalysis process that causes the partial decomposition of Ag_3PO_4 into Ag metallic and PO_4^{3-}. In ours study, after 25 min of exposure to visible light (Figure 4(a)), qualitative observations showed the sample changing color from yellow to gray, indicating the formation of Ag metallic. The strong PC performance of partially decomposed Ag_3PO_4 is noteworthy. Therefore, the experimental results indicated that $O_2^{•-}$ radicals and photogenerated h^+ participate in the photocatalytic process.

Based on these results, a possible PC mechanism for the degradation of RhB can be proposed. Initially, the Ag_3PO_4 (E_{gap} = 2.29 eV) is excited by visible light irradiation resulting in the formation of a e^-/h^+ pair. The e^-/h^+ pair immediately recombines or migrates towards the Ag_3PO_4 surface to serve as a redox source that subsequently reacts with the species adsorbed at the surface. The low photoluminescence emission intensity (**Supplementary Information Figure S4**) of Ag_3PO_4 —maximum emission is at 446 nm— indicates a low

recombination rate of the charge carriers, which favors PC activity. Consequently, the photogenerated e^- can react with O_2 to produce $O_2^{\cdot-}$, that then reacts with RhB. The photogenerated h^+ can react directly with RhB adsorbed on the Ag_3PO_4 surface to form degradation products. Other reactive oxygen species (ROS) including $HO_2^{\cdot}$ radicals and hydrogen peroxide (H_2O_2) can be formed by subsequent reactions [2, 56].
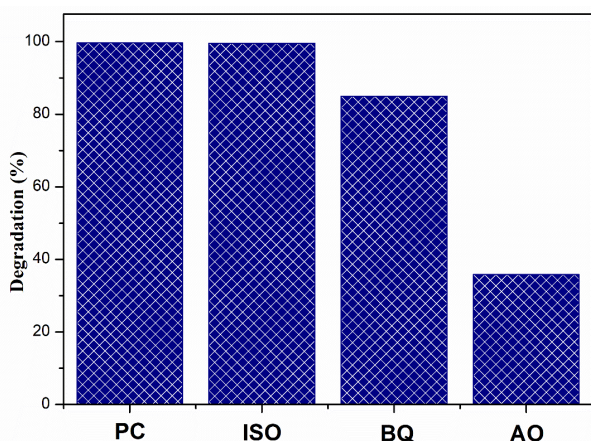

Fig. 5. Photocatalytic experiments without (PC) and with different scavengers (ISO, BQ, and AO).

Antibacterial activity measurements

Figure 6 shows the antibacterial effects of Ag_3PO_4 powder on MRSA inhibition as a function of concentration. Coincident values (62.5 µg/mL) of MIC and MBC were obtained for Ag_3PO_4 samples against MRSA planktonic cells. This concentration completely inhibited the growth of the MRSA colony. A significant reduction (from approximately 9.3 log10 CFU/mL to 4.5 log10 CFU/mL) compared to the control was observed at sub-MIC (31.2 µg/mL) concentrations. The inset in Figure 6 shows the morphology of an MRSA cell after interaction with Ag_3PO_4.
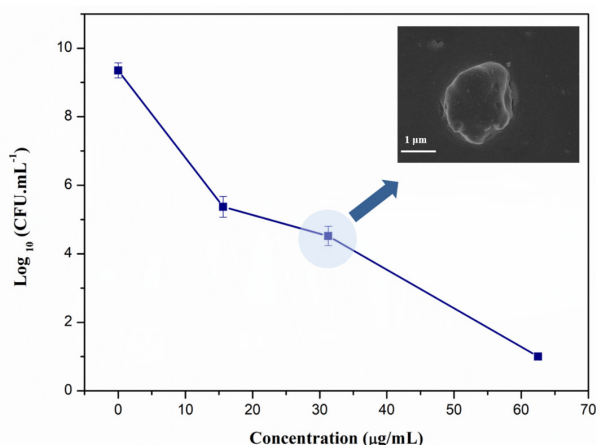

Fig. 6. Summary of log10 CFU/mL values obtained for different concentrations of Ag_3PO_4. The inset shows FE-SEM image of an MRSA cell exposed to sub-MIC concentrations of Ag_3PO_4.

Figure 7 details the interaction between the MRSA cells and Ag_3PO_4 powders. The FE-SEM images of untreated MRSA cells (control) show a preserved morphology with large numbers of cell aggregates (Figure 7(a-b)). The MRSA cells exposed to the Ag_3PO_4 powders showed irregular and altered morphology. Their appearance compared to that of the control sample was shriveled (dotted white circle in Figure 7(c-d)). Moreover, there are fewer cells in Figure 7(c) than in Figure 7(a). These images show that Ag_3PO_4 powders induce severe damage to MRSA cell morphology even at sub-MIC concentrations and confirm the antibacterial effect of Ag_3PO_4 powder.

The bactericide properties of Ag_3PO_4 are usually associated with the release of dissolved Ag^+ ions because Ag_3PO_4 is slightly soluble in aqueous solutions (0.02 g/L at 25 °C) [2-16]. For example, Baďurová et al. [16] investigated the photoinduced antimicrobial properties of Ag_3PO_4 against Escherichia coli (E. coli) and MRSA and associated the observed activity with the release of Ag^+ ions from Ag_3PO_4 into the solution.

Silver ions have been extensively studied in the last decades as effective bacterial killing agents that show significant antibacterial activity against an exceptionally broad spectrum of bacteria. This occurs because the Ag^+ ions have a high affinity to the thiol groups of respiratory and transport proteins [23, 57-62]. FE-SEM images reveal the presence of Ag nanoparticles on the Ag_3PO_4 surface. The inhibitory mechanism of the Ag nanoparticles on bacteria is not fully understood; however, several studies attribute this effect primarily to the Ag^+ ions that are gradually released after the oxidation of Ag nanoparticles. Ag^+ ions are known to induce the generation of ROS in bacterial cells, which lead to cell death by altering lipids, DNA, and proteins [61, 63-65]. Several ROS can contribute to the bactericidal effect, including singlet oxygen ($^1O_2$), $O_2^{\cdot-}$, $OH^{\cdot}$, and H_2O_2 species [62, 63, 65].

Because Ag_3PO_4 is a photocatalyst with a narrow band gap of 2.29 eV, it can be activated using visible light irradiation to form photocatalytic ROS ($O_2^{\cdot-}$ radicals) as determined by the PC reaction mechanism. In our experiments, the antibacterial activity against MRSA was analyzed under natural light illumination in the laboratory and produced good bactericide activity compared with previous studies [13, 16, 61]. Wu et al. [12] demonstrated the importance of irradiation and observed improved bactericidal activity of Ag_3PO_4 nano/microcrystals against Bacillus subtilis and E. coli of under simulated visible light irradiation when compared results to dark conditions. However, these authors did not propose a bactericidal mechanism based on ROS.

Our observations suggest that the bacterial performance of the Ag_3PO_4 powders resulted from the combined effects of Ag^+ ions released from Ag_3PO_4 and $O_2^{\cdot-}$ photogenerated radicals that induced chemical reactions in the microorganisms and caused the death of the MRSA cells. Photosensitive compounds that produce ROS in the presence of light have been widely studied in the last decades because of their antimicrobial activity [66-69], and an emphasis has been placed on silver-containing compounds [14, 19, 40, 70]. Experimental results show that Ag_3PO_4 has great potential as a general antibacterial agent and indicate that Ag_3PO_4 holds great promise as an alternative to antibiotics against MRSA.

3. Material and Methods

Synthesis of Ag_3PO_4 powders

The Ag_3PO_4 powders were prepared at room temperature using a simple precipitation method, as described in our previous work [25]. Initially, 1×10^{-3} mol di-ammonium hydrogen phosphate ((NH_4)$_2HPO_4$, 98.6% purity, J.T. Baker) and 3×10^{-3} mol silver nitrate ($AgNO_3$, 99.8% purity, Vetec) were

individually dissolved in 25 and 75 mL of deionized water, respectively. Subsequently, the $AgNO_3$ solution was added to the $(NH_4)_2HPO_4$ solution under stirring. The obtained suspension was washed with deionized water several times to remove any remaining ions. Finally, the resultant yellow powder was dried in a laboratory oven at 60 °C for several hours. After, the as-synthesized Ag_3PO_4 sample was employed in the PC and antibacterial experiments.
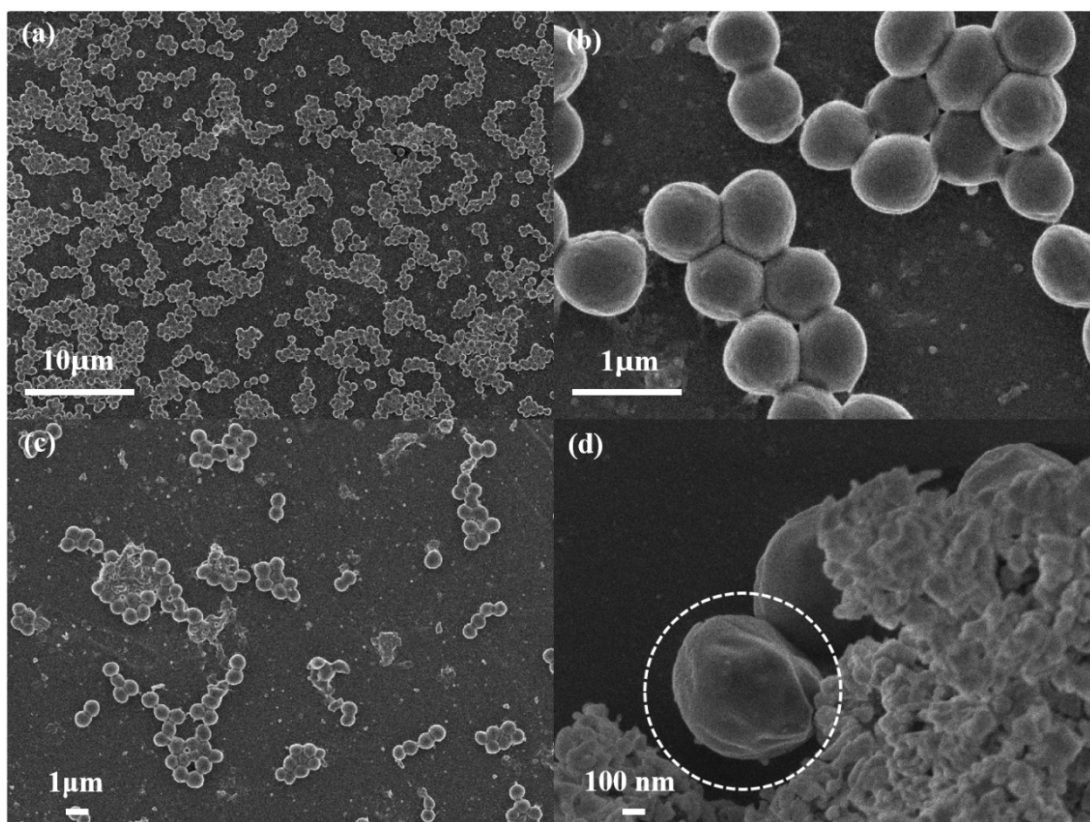

Fig. 7. FE-SEM images of an MRSA sample at different magnifications. (a−b) control sample without Ag_3PO_4 microcrystals, (c−d) samples previously treated with half-MIC concentration of Ag_3PO_4 microcrystals.

Characterization techniques

The structure of the Ag_3PO_4 powders was characterized using a D/Max-2500 PC Rigaku XRD device with Cu-Kα radiation (λ = 1.540 Å) in the 2θ range from 5−75° utilizing a scanning speed of 2°/min. Rietveld refinements were performed using the general structure analysis (GSAS) program with XRD measurements for 2θ ranging from 10−110° and a scanning speed of 0.2°/min. The FTIR spectrum was recorded at room temperature using an MB-102 Bomem−Michelson spectrophotometer in transmittance mode. The measurements were performed from 400−4000 cm^{-1} at a resolution of 4 cm^{-1} using potassium bromide pellets (KBr, ≥ 99% purity, Aldrich). The UV-vis DRS spectrum was obtained using a Cary 5G Varian spectrophotometer in diffuse reflection mode. The shapes and sizes of the Ag_3PO_4 particles were analyzed using a Supra 35-VP Carl Zeiss FE-SEM microscope operated at 15 kV. The photoluminescence spectrum was recorded at room temperature using a Monospec 27 monochromator (Thermal Jarrel Ash) coupled to an R446 photomultiplier (Hamamatsu Photonics. The krypton ion laser (Coherent Innova 200 K) with an excitation wavelength of 350 nm was maintained at 15 mW.

Photocatalytic activity measurements

The PC activity of the as-synthetized Ag_3PO_4 used for the degradation of rhodamine B (RhB, 95% purity, Mallinckrodt) dye in aqueous solution was tested under visible light irradiation in a photo-reactor containing six Philips TL-D 15W/54-765 fluorescent lamps, with emissions > 400 nm, at a constant temperature of 20 °C. The intensity of the lamps was of 24 W/m^2. The photocatalytic tests were evaluated by using of the RhB solution at pH 6.0 and initial concentration of 1×10^{-5} $mol.L^{-1}$. This dye has been used as a model compound in oxidation reactions as it presents a strong absorption in the visible region of the electromagnetic spectrum (λmax = 554 nm). First, 50 mg of Ag_3PO_4 was dispersed in 50 mL of RhB solution using a model 1510 Brason ultrasound bath for 15 min. The obtained suspension was placed in a PC system and stirred in the dark for 30 min. Subsequently, the suspension was illuminated, and 2 mL aliquots were collected at different intervals (0, 1, 3, 5, 7, 10, 15, 20, and 25 min) and centrifuged to remove the Ag_3PO_4 powder. Finally, variations in the maximum absorption band of these solutions were monitored by UV-vis absorbance spectra measurements using a Jasco spectrophotometer (model V-660).

To elucidate the PC mechanism responsible for the degradation of the RhB solution, different trapping experiments were performed to detect the reactive species as the reaction progressed. These trapping experiments used different scavengers, such as isopropanol (ISO), $((CH_3)_2CHOH$, 99.5%, Synth), p-benzoquinone (BQ) $(C_6H_4O_2$, 99%, Merck), and di-ammonium oxalate monohydrate (AO), $((NH_4)_2C_2O_4 \cdot H2O$, 99.5−101%, Merck). Before illuminating the mixtures, 0.25 mmol of each scavenger was added to the RhB solutions. The experiments were performed under conditions similar to those employed in the PC experiment described above.

Antibacterial activity measurements

The as-synthesized Ag_3PO_4 sample were also investigated for antibacterial activity against the Gram-positive bacterium MRSA. The antimicrobial activity of the Ag_3PO_4 powders was evaluated by determining the minimal inhibitory concentration (MIC) and minimum bactericidal concentration (MBC) toward planktonic cells for one reference strain from the MRSA American Type Culture Collection (ATCC 33591). The tests were performed according to the Clinical and Laboratory Standards Institute (CLSI) broth microdilution method (document M7-A7, 2006) [27].

The standard MRSA strain was streaked onto Mueller Hinton agar plates (Acumedia Manufactures Inc., Baltimore, MD, USA) and incubated at 37 °C for 24–48 h. One loopful of the fresh cells of the microorganism grown on the agar plates was then transferred to tryptic soy broth (TSB, Acumedia Manufactures, Inc. Baltimore, MD, USA) and incubated overnight in an orbital shaker (75 rpm) at 37 °C. The cells were harvested and washed twice with phosphate-buffered saline (PBS, pH 7.2) solution at 5000 × g for 5 min. The washed bacterial cells were resuspended in TSB, and the MRSA suspension was spectrophotometrically standardized to a final concentration of 107 CFU/mL by adjusting the optical density of the suspension. Subsequently, the adjusted inoculum suspension was diluted in the broth culture medium. Each well contained approximately 105 CFU/mL after inoculation with Ag_3PO_4.

To determine MICs and MBCs, MRSA was incubated in 96-well microtiter plates for 24 h at 37 ºC and exposed to two-fold serial dilutions of each of the Ag_3PO_4 solutions (1000–0.061 µg/mL) in the TSB culture medium. The positive controls were inoculated culture media without Ag_3PO_4 powders, and the uninoculated culture media were used as negative controls. The MICs were defined as the lowest concentrations of each sample that prevented the visible growth of a microorganism in an agar or broth dilution susceptibility test [27]. To determine the MBC values, aliquots from 10-fold serial dilutions (10^{-1}–10^{-8}) of each well were removed and inoculated (25 µL) in duplicate on a Mueller Hinton agar plate. After 24–48 h of incubation at 37 °C, the CFU/mL values were calculated, and log10 was transformed. The MBC values were defined as the lowest concentrations of each of the Ag_3PO_4 solutions without bacterial growth on the plates. The assays were performed in triplicate.

FE-SEM analysis

FE-SEM was used to examine the structure of the microorganisms and the interactions between the MRSA cells and Ag_3PO_4 powders. For this assay, after cultivation in TSB for 24 h, MRSA suspensions were spectrophotometrically standardized to a final concentration of 10^7 CFU/mL and placed on polystyrene disks in 24-well microplates (Orange Scientific, Belgium). After 90 min of incubation, the TSB medium was aspirated, and the non-adherent cells were washed twice with PBS. Subsequently, MBCs of the Ag_3PO_4 powders diluted in TSB were added to the microplates. After 24 h of incubation, the disks were fixed in 2 mL of glutaraldehyde solution for 1 h at room temperature, dehydrated with an ethanol series (70% ethanol for 10 min, 95% ethanol for 10 min, and 100% ethanol for 20 min), and dried for 20 min at room temperature. Prior to analysis, the disks were kept in a desiccator. Afterward, the disks were mounted onto Al stubs, coated with Au, and examined using FE-SEM.

4. Conclusions

In summary, Ag_3PO_4 was successfully synthesized using a simple precipitation approach. Its structure was analyzed using XRD and Rietveld refinement, which demonstrated the formation of a single-phase material with a body-centered cubic structure. The FTIR spectrum exhibited six modes associated with Ag_3PO_4 structure and revealed that the substance was locally ordered. In addition, the FE-SEM images showed that the Ag_3PO_4 sample was composed of several irregular spherical-like microparticles with an average size of approximately 300 nm that contained Ag nanoparticles on the surface. Direct oxidation by hole photogeneration and $O_2^{\cdot-}$ radicals was the primary photodegradation mechanism of the RhB dye under visible-light irradiation. The MIC of Ag_3PO_4, 62.5 µg/mL, was antibacterially active against MRSA cells. The experimental results showed that the morphology of MRSA cells was damaged by interaction with the Ag_3PO_4 powders, even at a subinhibitory concentration of 31.2 µg/mL. The mode of action of the Ag_3PO_4 was attributed to the synergetic effect of the Ag^+ ions released from Ag_3PO_4 and Ag nanoparticles and the $O_2^{\cdot-}$ radicals photogenerated by Ag_3PO_4 because of its narrow band gap of 2.2 eV. Therefore, it was possible to propose that the bactericidal activity of Ag_3PO_4 is the result of the combination of different mechanisms. Moreover, the high photo-absorption capability for visible light makes it possible for Ag_3PO_4 to be applied in different fields, such as photocatalyst and bacterial agent.

Supporting Information

The following files are available: **Rietveld refinement: lattice parameters, unit cell volume and atomic positions. Average particle size distribution. UV−Vis absorption spectroscopy analysis and photoluminescence.**

Author Contributions

Gleice Botelho: investigation, validation and writing – review & editing. Camila Cristina de Foggi: investigation, validation and visualization. Carlos Eduardo Vergani: supervision. Wyllamanney Silva Pereira: investigation and writing – original draft. Ricardo kaminishi dos Santos Júnior: investigation and validation. Elson Longo: conceptualization and supervision.

References and Notes

[1]   Chen, X.; Dai, Y.; Wang, X. *J. Alloys Compd.* **2015**, *649*,

910. **[Crossref]**

[2]. Martin, D. J.; Liu, G.; Moniz, S. J.; Bi Y.; Beale, A. M.; Ye, J.; Tang, *J. Chem. Soc. Rev.* **2015**, *44*, 7808. **[Crossref]**

[3] Yi, Z.; Ye, J.; Kikugawa, N.; Kako, T.; Ouyang, S.; Stuart-Williams, H.; Yang, H.; Cao, J.; Luo, W.; Li, Z.; Liu, Y.; Withers, R. L. *Nat. Mater.* **2010**, *9*, 559. **[Crossref]**

[4] Samal, A.; Baral, A.; Das, D. P. *Mater. Res. Found.* **2018**, *27*, 276. **[Crossref]**

[5] Tang, M.; Ao, Y.; Wang, C.; Wang, P. *Appl. Cat. B-Environ.* **2019**, *268*, 118395. **[Crossref]**

[6] Abroushan, E.; Farhadi, S.; Zabardasti, A. *RSC Adv.* **2017**, *7*, 18293. **[Crossref]**

[7] Hewer, T. L. R.; Machado, B. C.; Freire, R. S.; Guardani, R. *RSC Adv.* **2014**, *4*, 34674. **[Crossref]**

[8] Frontistis, Z.; Antonopoulou, M.; Petala, A.; Venieri, D.; Konstantinou, I.; Kondarides, D. I.; Mantzavinos, D. *J. Hazard. Mater.* **2017**, *323*, 478. **[Crossref]**

[9] Katsumata, H.; Taniguchi, M.; Kaneco, S.; Suzuki, *T. Catal. Commun.* **2013**, *34*, 30. **[Crossref]**

[10] Seo, Y.; Yeo, B.-E.; Cho, Y. S.; Park, H.; Kwon, C.; Huh, Y.-D. *Mat. Lett.* **2017**, *197*, 146. **[Crossref]**

[11] Liu, J.-K.; Luo, C.-X.; Wang, J.-D.; Yang, X.-H.; Zhong, X.-H. *Cryst. Eng. Comm.* **2012**, *14*, 8714. **[Crossref]**

[12] Wu, A.; Tian, C.; Chang, W.; Hong, Y.; Zhang, Q.; Qu, Y.; Fu, H. *Mater. Res. Bull.* **2013**, *48*, 3043. **[Crossref]**

[13] Piccirillo, C.; Pinto, R. A.; Tobaldi D. M.; Pullar R. C.; Labrincha J. A.; Pintado, M. M. E., Castro, P. M. L. *J. Photochem. Photobiol. A* **2015**, *296*, 40. **[Crossref]**

[14] Liu, B.; Xue, Y.; Zhang, J.; Han, B.; Zhang, J.; Suo, X.; Mu, L.; Shi, H. *Environ. Sci.: Nano.* **2017**, *4*, 255. **[Crossref]**

[15] Panthi, G.; Ranjit, R.; Kim, H.-Y.; Mulmi, D. D. *Optik.* **2018**, *156*, 60. **[Crossref]**

[16] Baďurová, K.; Monfort, O.; Satrapinskyy, L.; Dworniczek, E.; Gościniak, G.; Plesch, G. *Ceram. Int.* **2017**, *43*, 3706. **[Crossref]**

[17] Graffunder, E. M.; Venezia, R. A. *J. Antimicrob. Chemother.* **2002**, *49*, 999. **[Crossref]**

[18] De Foggi, C. C.; De Oliveira, R. C.; Fabbro, M. T.; Vergani, C. E.; Andres, J.; Longo, E.; Machado, A. L. *Cryst. Growth. Des.* **2017**, *17*, 6239. **[Crossref]**

[19] De Foggi, C. C.; Fabbro, M. T.; Santos, L. P.; De Santana Y. V.; Vergani, C. E.; Machado, A. L.; Cordoncillo, E.; Andrés, J.; Longo, E. *Chem. Phys. Lett.* **2017**, *674*, 125. **[Crossref]**

[20] Assis, M. D.; Robeldo, T.; De Foggi, C. C.; Kubo, A.; Mínguez-Veja, G.; Condoncillo, E.; Beltran-Mir, H.; Torres-Mendieta, R.; Andrés, J.; Oliva, M.; Vergani, C. E.; Barbugli, P. A.; Camargo, E. R.; Borra, R. C.; Longo, E. *Sci. Rep.* **2019**, *9*, 1. **[Crossref]**

[21] Wady, A. F.; Machado, A. L.; De Foggi, C. C.; Zamperini, C. A.; Zucolotto, V.; Moffa, E. B.; Vergani, C. E. *J. Nanomater.* **2014**, 128. **[Crossref]**

[22] Machado, T. R.; Macedo, N. G.; Assis, M.; Doñate-Buendia, C.; Mínguez-Veja, G.; Teixeira, M. M.; Foggi, C. C.; Vergani, C. E.; Beltrán-Mir, H.; Andrés, J.; Cordoncillo, E.; Longo, E. *ACS Omega* **2018**, *3*, 9880. **[Crossref]**

[23] Li, W.-R.; Sun, T.-L.; Zhou, S.-L.; Ma, Y.-K.; Shi, Q.-S.; Xie, X.-B.; Huang, X.-M. *Int. Biodeterior. Biodegrad.* **2017**, *123*, 304. **[Crossref]**

[24] Rai, M.; Yadav, A.; Gade, A. *Biotechnol. Adv.* **2009**, *27*, 76. **[Crossref]**

[25] Botelho, G.; Sczancoski, J. C.; Andres, J.; Gracia, L.; Longo, E. *J. Phys. Chem. C* **2015**, *119*, 6293. **[Crossref]**

[26] Botelho, G.; Andres, J.; Gracia, L.; Matos, L. S.; Longo, E. *ChemPlusChem.* **2016**, *81*, 202. **[Crossref]**

[27] CLSI, Methods for dilution antimicrobial susceptibility tests for bacteria that grow aerobically. In Standard - Seventh Edition, Wayne PA, 2006; Vol. M7-A7.

[28] Masse, R.; Tordjman, I.; Durif, A. *Z. Kristallog.* **1976**, *144*, 76. **[Crossref]**

[29] Chai, B.; Li, J.; Xu, Q. *Ind. Eng. Chem. Res.* **2014**, *53*, 8744. **[Crossref]**

[30] Dong, P.; Wang, Y.; Cao, B.; Xin, S.; Guo, L.; Zhang, J.; Li, F. *Appl. Catal., B.* **2013**, *132*, 45. **[Crossref]**

[31] Yan, T.; Guan, W.; Tian, J.; Wang, P.; Li, W.; You, J.; Huang, B. *J. Alloys Compd.* **2016**, *680*, 436. **[Crossref]**

[32] Jastrzębski W.; Sitarz M.; Rokita M.; Bułat K. *Spectrochim. Acta, Part A* **2011**, *79*, 722. **[Crossref]**

[33] Ayed, B. *C. R. Chim.* **2012**, *15*, 603. **[Crossref]**

[34] Mroczkowska, M.; Nowinski, J. L.; Zukowska G. Z.; Mroczkowska A.; Garbarczyk J. E.; Wasiucionek M.; Gierlotka, St. *J. Power Sources.* **2007**, *173*, 729. [Crossref]

[35] Nyquist, R. A.; Kagel, R. O. Infrared Spectra of Inorganic Compounds. 1th ed. Academic Press, 1971.

[36] Choudhary, B. P.; Singh, N. B. *J. Non-Cryst. Solids.* **2016**, *440*, 59. **[Crossref]**

[37] Ma, J.; Liu, Q.; Zhu, L.; Zou, J.; Wang, K.; Yang, M.; Komarneni, S. *Appl. Catal., B.* **2016**, *182*, 26. **[Crossref]**

[38] Longo, E.; Cavalcante, L. S.; Volanti, D. P.; Gouveia, A.; Longo, V.; Varela, J. A.; Orlandi, M. O.; Andrés, J. *Sci. Rep.* **2013**, *3*, 1676. **[Crossref]**

[39] Andrés, J.; Gracia, L.; Gonzalez-Navarrete, P.; Longo, V. M.; Avansi Jr, W.; Volanti, D. P.; Ferrer, M. M.; Lemos, P. S.; La Porta, F. A.; Hernander, A. C.; Longo, E. *Sci. Rep.* **2014**, *4*, 5391. **[Crossref]**

[40] Longo, V. R. M.; De Foggi, C. C.; Ferrer, M. M.; Gouveia, A.; André, R. S.; Avansi, W.; Vergani, C. E.; Machada, A. L.; Andrés, J.; Cavalcante, L. S.; Hernandes, A. C.; Longo, E. *J. Phys. Chem. A* **2014**, *118*, 5769. **[Crossref]**

[41] Longo, E.; Volanti, D. P.; Longo, V. R. M.; Gracia, L.; Nogueira, I. C.; Almeida, M. A.; Pinheiro, A. N.; Ferrer, M. M.; Cavalcante, L. S.; Andrés, J. *J. Phys. Chem. C* **2014**, *118*, 1229. **[Crossref]**

[42] De Oliveira, R. C.; Zanetti, S. M.; Assis, M.; Penha, M.; Mondego, M.; Cilense, M.; Longo, E.; Cavalcante, L. S. *J. Am. Ceram. Soc.* **2017**, *100*, 2358. **[Crossref]**

[43] Zhou, C.; Zhao, Y.; Cao, J.; Lin, H.; Chen, S. *Appl. Surf. Sci.* **2015**, *351*, 33. **[Crossref]**

[44] Khan, M. E.; Cho, M. H. In: Naushad, M., Rajendran, S., Gracia, F. A., Vol. 25 in *Advanced Nanostructured Materials for Environmental Remediation, Springer*, 2019, 173. **[Crossref]**

[45] Wood, D. L.; Tauc, J. *Phys. Rev. B.* **1972**, *5*, 3144. **[Crossref]**

[46] Tolvaj, L.; Mitsui, K.; Varga, D. *Wood Sci. Technol.* **2011**, *45*, 135. **[Crossref]**

[47] Qi, X.; Gub, M.; Zhua, X.; Wuc, J.; Wub, Q.; Longb, H.; Heb, K.; *Mater. Res. Bull.* **2016**, *80*, 215. **[Crossref]**

[48] Saud, P. F.; Pant, B.; Ojha, G. P.; Kim, D-U.; Kuk, Y-S.; Park,S-J.; Park, M.; Kim, H-Y. *J. Environ. Chem. Eng.* **2017**, *5*, 5521. **[Crossref]**

[49] Wang, B.; Gu, X.; Zhao, Y.; Qiang, Y. *Appl. Surf. Sci.* **2013**, *283*, 396. **[Crossref]**

[50] Wang, Z.; Iv, J.; Dai, K. Lu, L.; Liang, C.; Geng, L. *Mater. Lett.* **2016**, *169*, 250. **[Crossref]**

[51] Ghazalian, E.; Ghasemi, N.; Amani-Ghadim, A. *Mater. Res. Bull.* **2017**, *88*, 23. **[Crossref]**

[52] Sulaeman, U.; Suhendar, S.; Diastuti, H.; Riapanitra, A.; Yin, S. *Solid State Sci.* **2018**, *86*, 1. **[Crossref]**

[53] Ge, M. *Chin. J. Catal.* **2014**, *35*, 1410. **[Crossref]**

[54] Yang, X.; Cui, H.; Li, Y.; Qin, J.; Zhang, R.; Tang, H. *ACS Catal.* **2013**, *3*, 363. **[Crossref]**

[55] Yang, X.; Tang, H.; Xu, J.; Antonietti, M.; Shalom, M. *ChemSusChem.* **2015**, *8*, 1350. **[Crossref]**

[56] Ouyang, S.; Xu, H. New materials for degradation of organics. In: Schneider J, Bahnemann D, Ye J, Puma GL, Dionysiou DD, eds. Chapter 11 in Photocatalysis: fundamentals and perspectives. *Royal Society of Chemistry*, 2016.

[57] Zhao, G.; Stevens Jr., E. *Biometals.* **1998**, *11*, 27. **[Crossref]**

[58] Jiraroj, D.; Tungasmita, S.; Tungasmita, D. N. *Powder Technol.* **2014**, *264*, 418. **[Crossref]**

[59] Swathy, J. R.; Sankar, M. U.; Chaudhary, A.; Aigal, S.; Pradeep A. T. *Sci. Rep.* **2014**, 4, 7161. **https://doi.org/10.1038/srep07161**

[60] Yamanaka, M.; Hara, K.; Kudo, J. *Appl. Environ. Microbiol.* **2005**, *71*, 7589. **[Crossref]**

[61] Loza, K.; Diendorf, J.; Sengstock, C.; Ruiz-Gonzalez, L.; Gonzalez-Calbet, J.; Vallet-Regi, M.; Koller, M.; Epple, M. *J. Mater. Chem. B.* **2014**, *2*, 1634. **[Crossref]**

[62] Marambio-Jones, C.; Hoek, E. M. *J. Nanopart. Res*. **2010**, *12*, 1531. **[Crossref]**

[63] Choi, O.; Hu, Z. *Environ. Sci. Technol.* **2008**, *42*, 4583. **[Crossref]**

[64] Srikar, S. K.; Giri, D. D.; Pal, D. B.; Mishra, P. K.; Upadhyay, S. N. *Green Sustainable Chem.* **2016**, *6*, 34. **[Crossref]**

[65] Arya, G.; Sharma, N.; Mankamna, R.; Nimesh, S. Antimicrobial silver nanoparticles: future of nanomaterials. In: Prasad R. Vol 2 in *Microbial Nanobionics*. Springer; 2019. **[Crossref]**

[66] Adams, L. K.; Lyon, D. Y.; Alvarez, P. J. *Water Res.* **2006**, *40*, 3527. **[Crossref]**

[67] He, W.; Kim, H. -K.; Wamer, W. G.; Melka, D.; Callahan, J. H, Yin, J.-J. *J. Am. Chem. Soc.* **2013**, *136*, 750. **[Crossref]**

[68] Talebian, N.; Nilforoushan, M. R.; Zargar, E. B. *Appl. Surf. Sci.* **2011**, *258*, 547. **[Crossref]**

[69] Mathew, S.; Ganguly, P.; Rhatigan, S.; Kumaravel, V.; Byrne, C.; Hinder, S.; Bartlett, J.; Nolan, M.; Pillai, S. C. *Appl. Sci.* **2018**, *8*, 2067. **[Crossref]**

How to cite this article